ACS APPLIED ENERGY MATERIALS

www.acsaem.org Article

Investigating the Degradation of Nb_2O_5 Thin Films Across 10,000 Lithiation/Delithiation Cycles

Ilektra Andoni,[§] Joshua M. Ziegler,[§] Gaurav Jha, Chaitanya Avinash Gadre, Heriberto Flores-Zuleta, Sheng Dai, Shaopeng Qiao, Mingjie Xu, Vivian T. Chen, Xiaoqing Pan,* and Reginald M. Penner*

Cite This: *ACS Appl. Energy Mater.* 2021, 4, 6542−6552

Read Online

ACCESS | Metrics & More | Article Recommendations | Supporting Information

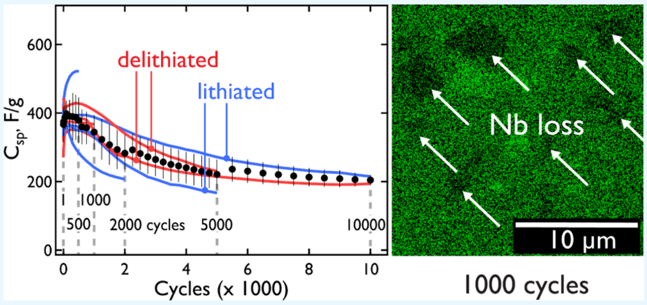

ABSTRACT: Nb_2O_5 is a Li^+ intercalation transition metal oxide that is of current interest for lithium ion battery and capacitor electrodes. For orthorhombic (T) Nb_2O_5 films prepared by electrophoretic deposition (EPD) and subjected to lithiation/delithiation cycling, a remarkably reproducible degradation process is observed. It is characterized by the onset of irreversible capacity loss from a baseline specific capacity, C_{sp}, of 400 (±50) F/g at 1000 (± 500) cycles. A gradual reduction of C_{sp} occurs during the ensuing 9000 cycles after which the C_{sp} stabilizes at 200 (±25) F/g. We investigate this degradation using six *ex situ* instrumental methods and more than 100 individual Nb_2O_5 films to characterize and understand the composition, atomic scale structure, chemical bonding, electrochemical, and electrical properties of these films during these 10,000 cycles. What emerges is a multidimensional picture of the degradation process in which the decline in C_{sp} occurs concurrently with an increase in the charge transfer resistance, a loss of crystalline order, and the dissolution of niobium from the film.

KEYWORDS: *niobium pentoxide, Nb_2O_5, degradation, lithium, battery, transition metal oxide*

■ INTRODUCTION

Transition metal oxides (TMOs) gradually lose their ability to reversibly intercalate/deintercalate metal ions (e.g., Li^+) after 500−1000 cycles. When TMOs are used as battery cathodes, this process causes irreversible capacity loss for the battery, necessitating its replacement. The degradation and failure mechanisms responsible for capacity loss are complex and commonly include three measurable changes:[1−5] (1) a loss of TMO crystallinity, (2) slowed ion intercalation/deintercalation and ion transport within the TMO, and (3) diminished electronic conductivity. In the cathodes of metal ion batteries, TMOs are mixed with conductive fillers to enhance electronic conductivity and binders to promote cohesion of the TMO layer. Mechanisms of degradation operating in such composite films are likely to involve these fillers and binders.[1−5] Since real battery electrodes contain these components, their participation in degradation is important to understand, but the complexity of these multicomponent systems with respect to degradation can be daunting.

In this study of degradation focusing on orthorhombic niobium (V) oxide (T-Nb_2O_5),[6−18] we simplify this problem in two ways. First, all binders and fillers are eliminated, ensuring that degradation pathways involving these extrinsic materials are removed. Second, electrophoretic deposition (EPD)[19] is used for synthesizing thin films of T-Nb_2O_5 films. We have recently reported[19] that EPD provides an unusually reproducible method for synthesizing thin films of T-Nb_2O_5. The use of many quasi-identical T-Nb_2O_5 films provides a means for studying the evolution of the structure and composition during the degradation process using tools including cyclic voltammetry, high-resolution transmission electron microscopy (HR-TEM), X-ray diffraction (XRD), scanning electron microscopy (SEM) coupled with energy-dispersive X-ray (fluorescence elemental) spectroscopy (EDS), electrochemical impedance spectroscopy (EIS), Raman microprobe spectroscopy, and X-ray photoelectron spectroscopy (XPS).

T-Nb_2O_5 is an interesting candidate TMO for this study because the orthorhombic polymorph shows unusually rapid Li^+ diffusion and intercalation/deintercalation kinetics[9,14,15,18,20−24]

$$Nb_2O_5 + xLi^+ + xe^- \rightleftharpoons Li_xNb_2O_5 \qquad (1)$$

Received: February 25, 2021
Accepted: June 11, 2021
Published: July 2, 2021

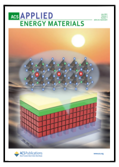

https://doi.org/10.1021/acsaem.1c00580

It also has a relatively high theoretical specific capacity, C_{sp}, of 202 mA h/g or 403 F/g for the 1.8 V voltage window used in this study. These values correspond to $x = 2$ in eq 1.[25]

T-Nb_2O_5 films of 60 (±20) nm thickness were prepared from colloidal suspensions of NbO_x using a two-step process involving EPD and calcination (Figure 1).[19] The reproducibility of these films in terms of their electrochemical response and the trajectory of the specific capacity over many lithiation/delithiation cycles are very good. For example, during repetitive potentiostatic cycling of these films at 200 mV/s, the C_{sp}, fades by ≈30% from 400 to 280 F/g after 2000 cycles.[19] Film to film dispersion of the C_{sp} is less than 15% from 0 to 10,000 cycles, providing the opportunity for *ex situ* investigation of the film structure (XRD, TEM, and SEM), chemical composition (EDS and XPS), local bonding environments (Raman spectroscopy), and electrochemical metrics (via *in situ* EIS). The focus of this study is the mechanisms responsible for the degradation causing this irreversible capacity loss.

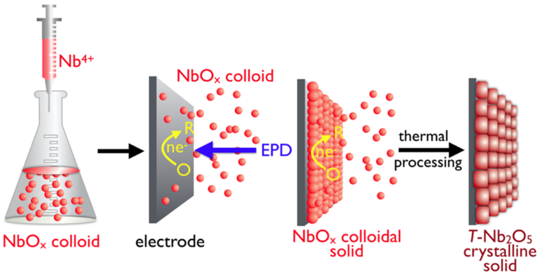

Figure 1. Schematic diagram of EPD of NbO_x and subsequent processing to obtain T-Nb_2O_5.

■ RESULTS AND DISCUSSION

Ex Situ TEM Analysis of Degrading T-Nb_2O_5 Films. T-Nb_2O_5 films were cycled voltammetrically between 1.3 and 3.1 V *versus* Li/Li^+ at 200 mV/s for 10,000 cycles (Figure 2a). Even at this rapid charge/discharge rate, corresponding to a C-rate exceeding 400, the voltammetry of fresh films is characterized by a reversible cathodic lithiation peak at 1.57 V and an anodic delithiation peak at 1.75 V—as previously observed for Nb_2O_5 films[14,15,20,23] and nanostructures.[6,8,10,12]

Fresh T-Nb_2O_5 films produce C_{sp} values of 360−420 F/g (Figure 2b), approaching the theoretical maximum value of 403 F/g. Beyond 1000 cycles, C_{sp} smoothly decreases by 50% to 200 F/g at 10,000 cycles (Figure 2b). The reproducibility of these cycle stability curves is excellent, as evidenced by the error bars that show ±1σ for up to 12 different films. This cycle stability equals or exceeds that reported for Nb_2O_5 in previous studies.[14,15,21,23,24,26] This suggests that some degradation channels are eliminated by the omission of conductive fillers and binders and possibly by the nanoscopic dimensionality of the film thickness. Understanding the origins of this irreversible capacity loss is the goal of this paper.

The evolution of crystallinity and crystal structure of T-Nb_2O_5 films were tracked by *ex situ* TEM during the degradation process by halting the cycling of films and preparing cross-sectional specimens for TEM analysis. Twelve T-Nb_2O_5 films, corresponding to the twelve C_{sp} *versus* cycle

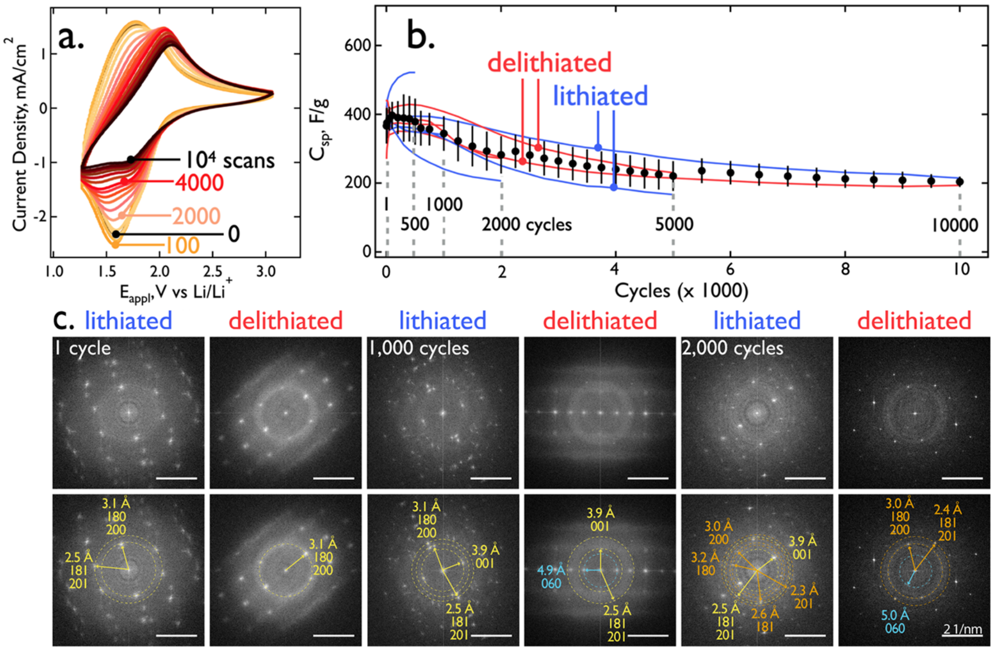

Figure 2. Electrochemical and *ex situ* TEM analysis of T-Nb_2O_5 films. (a) Voltammetric cycling of a 60 nm T-Nb_2O_5 film at 200 mV/s in 1.0 M $LiClO_4$/PC showing a loss of capacity coupled with a positive shift in the reversible potential by 100−200 mV across 10,000 scans. (b) Plots, for twelve T-Nb_2O_5 films, of C_{sp} *vs* the number of lithiation/delithiation cycles. Data points (black) are average C_{sp} values with ±1 σ error bar. Blue and red data were used to acquire TEM data for lithiated and delithiated films, respectively. (c) Raw FFTs of atomic resolution TEM images (top) are paired with assignments (bottom) for lithiated and delithiated films at 1, 1000, and 2000 cycles. Changes in the major three lithiation planes, 001 (3.9 Å), 180/200 (3.1 Å), and 181/201 (2.5 Å), are tracked. Yellow indices represent the periodicities corresponding to literature T-Nb_2O_5 *d*-spacings. Orange indices correspond to distortions of literature *d*-spacings either due to lithiation (increase in *d*-spacing) or damage to the crystal integrity (decrease in *d*-spacing). Blue indices track the appearance of a 060 (4.9 Å) family of planes which have not been shown to contribute to lithiation in T-Nb_2O_5.

data sets shown in Figure 2b, were used for the preparation of the samples studied by TEM. Black data points and error bars are mean values and standard deviations, respectively, for C_{sp}, showing the reproducibility of the electrochemical energy storage properties of these films. Cross-sectional TEM studies were also conducted on thin films after 0, 1, 1000, 2000, 5000, and 10,000 voltammetric lithiation/delithiation cycles (Figures 2c and 3). TEM data for 5000 cycle films is omitted here because these films were indistinguishable from 2000 cycle samples. Two samples were examined at each of these junctures corresponding to the lithiated (1.3 V *vs* E_{Li/Li^+}) and delithiated (3.1 V *vs* E_{Li/Li^+}) states, as indicated.

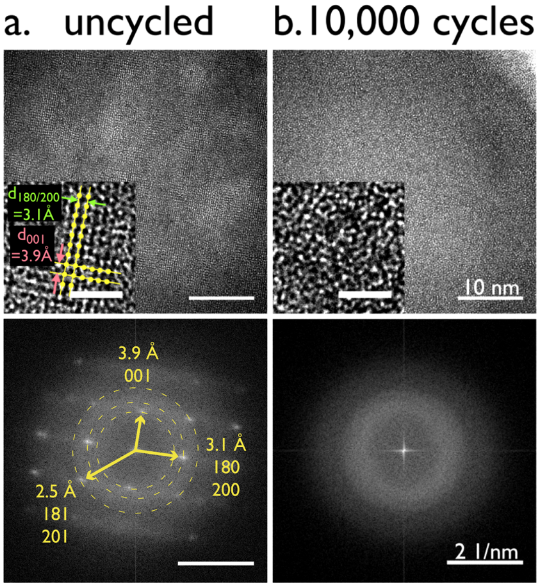

Figure 3. Real space and Fourier-transformed TEM images. (a,b) TEM images shown in real space (top) and after the application of an FFT (bottom) for (a) a freshly prepared, uncycled T-Nb_2O_5 film and (b) a film cycled 10,000 times. (a) Inset shows the niobium sublattice at higher magnification. (b) T-Nb_2O_5 film cycled 10,000 times at 200 mV/s is completely amorphous. FFTs of these images show no prominent reflections, and no atomic order is seen at higher magnification (inset). The distance bar for the inset images is 2 nm.

The niobium sublattice can be seen in HR-TEM images of the as-prepared films (Figure 3a, top). However, the crystallinity and structure of this material is more readily determined by evaluating fast Fourier transforms (FFTs) of the real-space TEM images, as shown in Figure 3a (bottom). In the bottom image of Figure 3a, the FFT shows prominent peaks produced by the 001, 180/200, and 181/201 periodicities present in the TEM image. At higher magnification (Figure 3a, top inset), (001) and (180/200) planes of Nb atoms are resolved. In contrast, after 10,000 cycles, no evidence of the crystalline structure is observed in either real space or FFTs of the HR-TEM images (Figure 3b). The integrity of the orthorhombic lattice is more easily evaluated from FFTs of the real space TEM data, and FFTs are analyzed exclusively below.

Correlation of Specific Capacity with Cycling and Local Film Crystallinity. Simon and co-workers[23] collected XRD data of the T-Nb_2O_5 film as a function of lithiation potential. They observed that reflections for the 001 (3.9 Å), 180 (3.1 Å), and 181 (2.5 Å) planes shifted to higher *d*-spacing values when Li^+ was inserted into the lattice. From their study, it can be inferred that these planes provide the necessary pathways for Li^+ to intercalate and translate through the material.[23] These planes are readily identified in the FFT of the uncycled film (Figure 3a, bottom).

The progressive loss of crystallinity of T-Nb_2O_5 films with cycling is evidenced by the changes seen in these planes at 1 cycle, 1000 cycles, and 2000 cycles (Figure 2c). This analysis focuses on the major three planes, 001 (3.9 Å), 180/200 (3.1 Å), and 181/201 (2.5 Å) (Figure 2c, yellow). The remaining unmarked reflections are predominantly derived from the same families of planes but are much weaker in intensity. It should be noted that the resolution of these TEM images is insufficient to permit the 180 (3.14 Å) and 200 (3.09 Å) or the 181 (2.45 Å) and 201 (2.43 Å) planes to be resolved. Instead, the *d*-spacings of each appear as 3.1 and 2.5 Å, respectively.

After the first lithiation of the pristine T-Nb_2O_5 thin film sample (Figure 2c, 1 cycle), the presence of both shifted and unshifted reflections is seen, revealed by the doubling of the reflections. This implies that lithiation of the lattice was incomplete and both lithiated and delithiated domains in the film are contributing to the TEM image in this region. Multiple reflections and distortions are also observed for the 180/200 (3.1 Å) and 181/201 (2.5 Å) planes, but the measured shifts in these reflections are too small to significantly deviate from the literature *d*-spacings. While the lithiated sample has a distorted orthorhombic structure, it has not lost significant crystallinity in the first lithiation. As the sample is delithiated (Figure 2c, one cycle), the FFT shows that the sample returns to the initial orthorhombic state. The FFT shows the presence of only the 180/200 (3.1 Å) plane, and doubled peaks signaling the presence of lithiated and delithiated domains are no longer visible.

By the 1000th cycle, the distortions in the lattice are more evident in the lithiated FFT. While the reflections for the three major lithiation planes are indexed with literature values, multiple double reflections can be seen with slight deviations from the literature distances. Blurring of the bright reflections into rings can be attributed to a decrease in the crystallite size and random orientation of the crystals approaching a more polycrystalline sample as the stress of de/lithiation damages the crystal integrity. As the sample is delithiated, the family of planes with a *d*-spacing of 4.9 Å (Figure 2c, blue) can be assigned to the 060 plane, but this plane has not been shown to contribute to lithiation in T-Nb_2O_5.

After 2000 cycles, the lattice is severely distorted. In the lithiated sample, the *d*-spacings for the 180/200 and 181/201 planes show significant deviations from the literature values. Reflections that do not conform to the orthorhombic model are proposed to be the result of minor to severe deformations from the parent orthorhombic structure (Figure 2c, orange). For the 181/201 (2.5 Å) plane, reflections show both an increase in the *d*-spacing (2.6 Å) which can be attributed to expansion due to lithiation and a decrease in the *d*-spacing (2.3 Å) which could be due to degradation of the crystallinity. In the delithiated state, all the visible planes do not revert back to the original orthorhombic structure after thousands of cycles but appear to remain contracted as compared to literature values. By 2000 cycles, the distortions in the *d*-spacings are much more severe and irreversible. Although faint, the family of reflections with 5.0 Å *d*-spacing corresponding to the 060 plane is again visible at 2000 cycles.

As the films are cycled beyond 2000 cycles, several reflections show the orthorhombic structure (3.9, 3.1, and 2.5 Å) (Figure 2c, yellow), but most of the reflections show distorted orthorhombic planes (3.2, 3.0, 2.3, 2.4, and 2.6 Å) (Figure 2c, orange) or orthorhombic planes that do not contribute to lithiation (4.9 and 5.0 Å) (Figure 2c, blue). The distorted reflections are also doubled and blurred, representing a small crystallite size, random crystal orientation, and nonuniform lithiation throughout the film. Finally, after 10,000 cycles, the distortions increase to the point that the whole structure breaks down and only amorphous Nb_2O_5 remains (Figure 3b). To summarize, as the lithiation/delithiation progresses, the T-Nb_2O_5 structure slowly degrades to a completely amorphous structure, destroying the lowest energy pathways for Li^+ to traverse through this lattice (Table 1). In addition to impeding Li^+ transport in the lattice, the loss of crystallinity can be expected to reduce the rate of Li^+ intercalation and to increase the electrical resistance of the T-Nb_2O_5. These TEM observations demonstrate that the observed capacity fade (Figure 2b) occurs in parallel with a monotonic loss of lattice integrity and, eventually, the complete loss of the orthorhombic crystal structure.

Table 1. Evolution of the T-Nb_2O_5 Structure with Cycling

cycle	lithiated	delithiated
pristine		orthorhombic
1	expanded orthorhombic	orthorhombic
1000	disoriented orthorhombic	deformed orthorhombic
2000	deformed and disoriented orthorhombic	highly deformed and disoriented orthorhombic
10000	amorphous	amorphous

Delamination of the T-Nb_2O_5 Film from the FTO. In parallel with the loss of crystallinity seen in the TEM data of Figures 2 and 3, cross-sectional TEM images of the T-Nb_2O_5 film/fluorine-doped tin oxide (FTO) interface (Figure 4) reveal that a second process is occurring that is likely to depress C_{sp}. This is the delamination of the film from the FTO current collector, resulting in the formation of cavities (Figure 4, white regions). For the pristine T-Nb_2O_5 film, a tight interface is observed (Figure 4a). However, small cavities are already observed after just one lithiation/delithiation cycle (Figure 4b), and these cavities pervade most of the interfaces after 1000 cycles, extending for up to one micron (Figure 4c). Strain between the FTO electrode and the T-Nb_2O_5 film is a likely cause for the loss of film adhesion to the FTO and the formation of cavities at this interface.

This progressive delamination of the film from the FTO conductor provides a second mechanism, in addition to the degradation of the T-Nb_2O_5 lattice itself, which can be expected to contribute to the increased electrical resistance at the FTO/film interface potentially contributing to a loss of C_{sp}.

SEM Images and EDS Elemental Mapping. Strain caused by the volume change produced by lithium intercalation/deintercalation is implicated in the degradation of the orthorhombic T-Nb_2O_5 lattice (Figures 2 and 3) and in the delamination of the film from the FTO current collector (Figure 4). On the other side of the film which is in contact with the electrolyte, the roughening and pitting of cycled T-Nb_2O_5 film surfaces are seen in *ex situ* SEM images (Figure 5). An EDS elemental map showing the Nb Lα1 peak reveals dark areas where the active material is no longer present. Pristine, uncycled films show a typical pebbled texture that derives from the deposition of colloidal Nb_2O_5 particles during EPD film growth (Figure 5a). These films show a quasi-uniform Nb EDS signal across the image (Figure 5d). After just one lithiation/delithiation cycle, cracking is observed (Figure 5b) and loss of Nb is seen at these cracks (Figure 5e). For films cycled 1000 times, pitting and flaking of the film surface are pronounced (Figure 5c) and Nb loss is colocalized with these defects (Figure 5f).

Bulk Crystallinity as a Function of Cycling. While TEM probes the localized crystalline structure of these films in nanometer-scale regions, XRD is capable of assessing the spatially averaged structure across a much larger, 100 micron- or millimeter-scale area, probed by the X-ray beam. Thus, TEM and XRD provide fully complimentary data on the evolving structure of these films as degradation occurs. To this end, grazing incidence XRD (GIXRD) was conducted on a series of T-Nb_2O_5 films across the same 10,000 cycle range explored by TEM and other techniques in this study.

The GIXRD pattern of the pristine, uncycled film aligns with the literature pattern for T-Nb_2O_5,[15,18,23] in agreement with the diffraction points seen in the FFT of the pristine film (Figure 3a, bottom) and tetragonal SnO_2 from the FTO (Figure 6a).[27] The three planes associated with the main lithiation pathways are tracked as a function of cycling (Figure 6b). The calculated *d*-spacings for the 001, 180/200, and 181/201 planes are 3.911, 3.099, and 2.438 Å, respectively, which agree with the *d*-spacing values measured from TEM. The crystallite size calculated using the Scherrer equation is approximately 20 nm.

After one cycle, GIXRD reflections are shifted to a smaller *d*-spacing for delithiated films and a larger *d*-spacing for lithiated

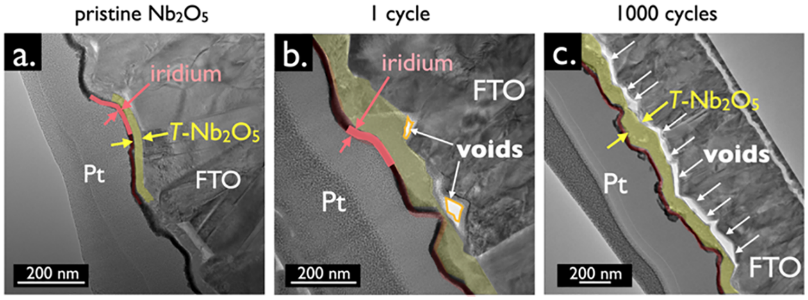

Figure 4. Cross-sectional TEM of the T-Nb_2O_5 film/FTO interface. (a) Pristine T-Nb_2O_5 film showing intimate contact between the film and the FTO. (b). After one lithiation/delithiation cycle, small voids (white outlined in orange) begin to open between the film and the FTO. (c). After 1000 cycles, delamination between the FTO and the film extends for up to one micron.

https://doi.org/10.1021/acsaem.1c00580
ACS Appl. Energy Mater. 2021, 4, 6542−6552

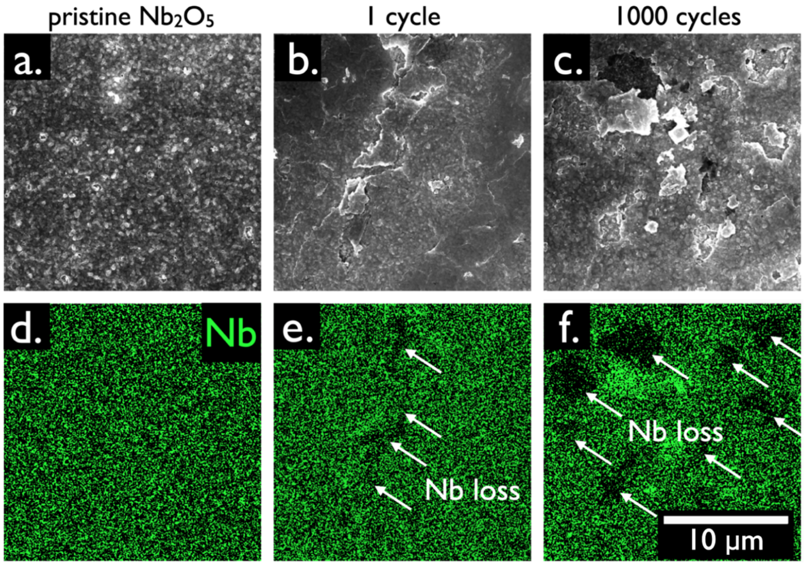

Figure 5. SEM (a−c) and EDS (d−f) analysis of T-Nb_2O_5 film surfaces. (a,d) Typical texture for pristine T-Nb_2O_5 films. EDS analysis of this region shows a quasi-uniform Nb signal (green). (b,e) After one lithiation/delithiation cycle, cracking of the film surface is observed. Such cracks also show loss of the Nb signal. (c,f) After 1000 cycles, pitting and flaking of the film surface are seen.

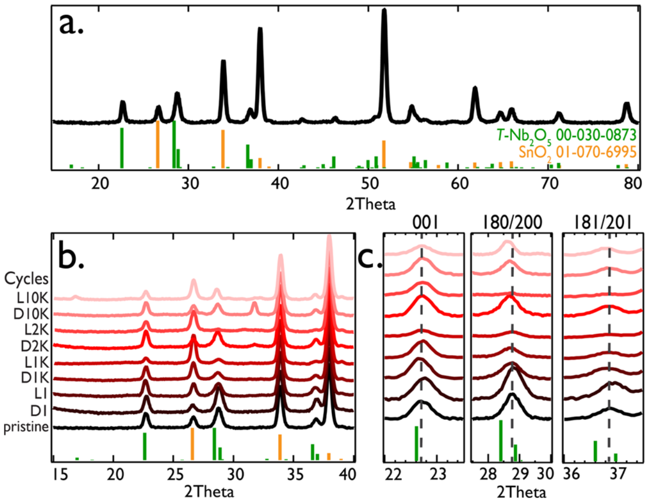

Figure 6. GIXRD data for T-Nb_2O_5 thin films on FTO. (a) GIXRD pattern for a pristine T-Nb_2O_5 film on FTO. T-Nb_2O_5 reflections are indexed in green, and tetragonal SnO_2 reflections from the FTO substrate are indexed in orange. (b) XRD patterns collected from 15 to 40° across 10,000 cycles. Delithiated films are denoted with a "D", and lithiated films are labeled with "L". GIXRD data for films cycled for 0 (pristine), 1, 1000, 2000, and 10,000 cycles are shown in both the lithiated and delithiated state. The reflection at 31.8° can be assigned to the cubic phase of SnO_2 from FTO, and the small reflection at 16.9° in the 10,000 cycle lithiated sample is assigned to the 130 plane of T-Nb_2O_5 with a *d*-spacing of 5.2 Å. (c) Expanded windows for the 001, 180/200, and 181/201 reflections showing changes in peak position as compared to the pristine sample (dashed line).

films (Figure 6b,c). Approximately, a 0.01 Å contraction/expansion is observed, which can account for the lack of significant change in the *d*-spacing measured by TEM between the pristine film and the one-cycle de/lithiated films (Figures 2c, 3a bottom, Figure 6b,c). Simon and co-workers[23] measured a 0.1 Å change in *d*-spacing with lithiation in T-Nb_2O_5 electrodes, suggesting nonuniform de/lithiation in the thin films observed here. Peak broadening from pristine films to films after one cycle can suggest that films are partially de/lithiated, and the XRD reflections represent both states of lithiation across the film (Figure 6c). Additionally, peak broadening could be due to a decrease in crystallite size which is seen in TEM by the blurring and doubling of diffraction spots (Figure 2c).

By 1,000 cycles, signs of degradation are noticeable, particularly in the lithiated films (Figure 6b,c). Very little peak shift occurs with lithiation and delithiation, suggesting that these lithiation pathways are starting to deteriorate. A slight increase in peak broadening, especially in the lithiated samples, continues to suggest that films are nonuniformly lithiated, as seen in TEM. Furthermore, the low intensity of T-Nb_2O_5 reflections hints at a decrease in the crystallinity of the film.[28]

At 2,000 and 10,000 cycles, there is virtually no change in *d*-spacing between the pristine film and the de/lithiated films except for the 180/200 plane which appears to remain lithiated even in the delithiated sample (Figure 6b,c). The intensity of the lithiated (Figure 6b,c) film after 2,000 cycles is so low that the 180/200 and 181/201 peaks appear amorphous. However, in contrast to the TEM data of Figure 3, GIXRD does not show that the films are amorphous after 10,000 cycles. However, in view of the fact that crystallinity of these films is substantially degraded at 1,000 and 2,000 cycles, the possibility exists that film delamination of the 10,000 cycle samples from the current collector occurred, preventing these films from cycling and preserving the crystallinity of these samples. This scenario is supported by the fact that little change in *d*-spacing and peak width is observed between the pristine film and the 10,000 cycle film samples. A decrease in cycle stability and little change in crystallinity hint that the delaminated portion of the film does not contribute to de/lithiation capacity.

Overall, these GIXRD data support the conclusion that in the bulk of these T-Nb_2O_5 films, lithiation pathways deteriorate as a function of cycling as evidenced by the loss of *d*-spacing changes—between lithiated and delithiated films—after 2,000 cycles. TEM hints that local regions within

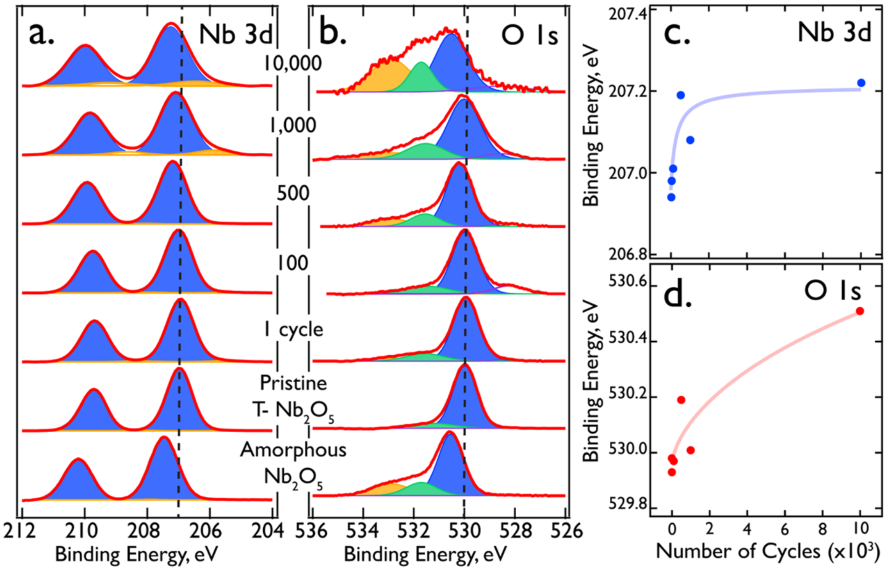

Figure 7. XPS analysis of delithiated T-Nb_2O_5 as a function of the number of lithiation/delithiation cycles. (a). Nb 3d high-resolution photoelectron spectra for five T-Nb_2O_5 samples subjected to 1−10,000 cycles compared with pristine and amorphous (unannealed) samples. Blue fittings correspond to Nb^{5+}, and orange corresponds to Nb^{4+}. (b) Oxygen 1s photoelectron spectra for the same samples shown in (a). In these spectra, blue corresponds to lattice O^{2-}, green corresponds to nonlattice oxygen, and orange corresponds to adsorbed OH^- and H_2O. (c) Plot of Nb 3d binding energy *vs* number of cycles, (d) plot of O 1s binding energy *vs* number of cycles.

these films are "trapped" in a lithiated or delithiated state by 2,000 cycles, accounting for the broad peaks seen in GIXRD that average out to *d*-spacing values close to those of an uncycled film. Between 2,000 and 10,000 cycles, the lack of amorphization in GIXRD and low capacity suggest that large areas of the films delaminate to the point where they can no longer contribute to de/lithiation and stop degrading. However, TEM shows that regions that do remain in contact become fully amorphous by 10,000 cycles.

***Ex Situ* XPS Analysis of Surface Chemical Composition.** In 2016, Yu and co-workers[13] used *ex situ* XPS to monitor the oxidation state of a Nb_2O_5 nanosheet anode as a function of its equilibrium potential in 1 M $NaClO_4$ in a mixture of ethylene carbonate and propylene carbonate. They found that upon intercalation of sodium cations, Nb 3d peaks shift to a lower binding energy due to conversion of most Nb^{5+} centers to Nb^{4+} centers and then revert to higher binding energy upon deintercalation.[13] Luo and co-workers[29] also investigated the sodiation of T-Nb_2O_5 using *ex situ* XPS over the course of 2 cycles and noted that a full conversion of the Nb metal centers between the charged and discharged states was not observed. Rather, the Nb centers cycled between two charge states, $Nb^{+4.92}$ and $Nb^{+4.10}$, suggesting that a mix of Nb valences is present in the sample throughout the sodiation process. These studies focused on the initial intercalation and deintercalation cycles for Nb_2O_5.

Few investigations report the XPS analysis of the surface chemical state of T-Nb_2O_5 caused by long-term cycling. Nakajima and co-workers[30] looked at different states of charge over the course of 10 lithiation/delithiation cycles for T-Nb_2O_5 films. These authors reported a reversible shift of 0.5 eV to lower binding energies for the Nb 3d peaks when the sample was fully lithiated. Subsequent cycling led to the disappearance of clear peaks in the Nb 3d region. In the O 1s spectra, lithiation caused an irreversible 2 eV shift in the lattice O^{2-} peak from 531.3 to 533.3 eV, which recovered to 533.0 eV upon delithiation.[30]

XPS data were acquired for delithiated films as a function of the number of lithiation/delithiation cycles (Figure 7a,b). The as-synthesized but unannealed Nb_2O_5 films show Nb 3d peaks (Figure 7a, "Amorphous") with binding energies of 207.47 and 210.21 eV assigned to Nb $3d_{5/2}$ and $3d_{3/2}$, respectively, in agreement with literature values for amorphous Nb_2O_5 films.[31] Calcining introduces oxygen vacancies to T-Nb_2O_5 films (Figure 7a, "Pristine"), and this is demonstrated by the Nb/O stoichiometry of 29.9% Nb and 70.1% O, corresponding to a stoichiometry of $Nb_2O_{4.7}$ for the orthorhombic films. Nb $3d_{3/2}$ and Nb $3d_{5/2}$ peaks are shifted lower by ≈500 meV in the films annealed at 600 °C, compared with the amorphous material. These shifts are similar to those seen by others who have investigated Nb_2O_5 with oxygen vacancies resulting from elevated annealing temperatures.[32,33] For example, Atak investigated the effect of heat treatment on the optical, structural, electrochromic, and bonding properties of 0.125 inch-thick T-Nb_2O_5 films and observed a negative shift of 300 meV upon annealing the as-synthesized material at 600 °C.[32] The O 1s region in the pristine film (Figure 7b, "Pristine") shows the presence of three peaks at 530.0, 531.0, and 532.1 eV which correspond to lattice O^{2-}, nonlattice oxygen, and adsorbed −OH and H_2O, respectively.[34] Film stoichiometry was determined using the peaks for lattice O^{2-} and nonlattice oxygen. Atak and co-workers[32] reported a negative shift by 0.4 eV in the binding energy of the O 1s peaks after annealing their films to 600 °C, which is also seen here for films transitioning from amorphous Nb_2O_5 to crystalline T-Nb_2O_5.

After one lithiation/delithiation cycle, a small shift in Nb 3d peaks by 40 meV is observed (Figure 7a, "one cycle"). This shift is much smaller than the ≈0.5 eV shift to lower binding energy that has been reported when Nb_2O_5 films are lithiated,[31] but it is in the same direction. This implies that it could be a consequence of irreversible Li insertion into the T-Nb_2O_5. In the O 1s spectrum (Figure 7b, "one cycle"), the lattice O^{2-} peak is also shifted negatively by 30 meV. This is interesting because the irreversible shift seen by Nakajima and co-workers[30] is absent here. As the T-Nb_2O_5 is cycled, Nb 3d peaks steadily shift to higher binding energies, approaching values seen in amorphous films (Figure 7a,c). The O 1s spectrum displays similar behavior, with both lattice O^{2-} and nonlattice oxygen peaks shifting to higher binding energies (Figure 7b,d). The observed evolution of O 1s and Nb 3d are consistent with an increasing contribution of high valance Nb^{5+} as cycling progresses. In parallel with these shifts, both Nb 3d and O 1s peaks also broaden considerably. For example, in the case of the Nb 3d peaks (Figure 7a), the line width of the Nb 3d peaks for pristine T-Nb_2O_5 is 0.95 eV, and these peaks broaden to 1.35 eV after 10,000 cycles, suggesting an increase in the heterogeneity of the Nb chemical state. Even more dramatic broadening of the O 1s peak (Figure 7b) is caused by increased contributions from nonlattice O and adsorbed H_2O and OH^- species.

The evolution of the XPS spectrum as a result of cycling can be accounted for by a combination of two processes: First, T-Nb_2O_5 films become progressively more amorphous with cycling causing line widths to broaden for both Nb 3d and O 1s peaks. The amorphous, as-synthesized state of Nb_2O_5 has an oxidation state of Nb^{5+}. Calcination imparts crystallinity while also introducing oxygen vacancies, resulting in a mixture of Nb^{4+} and Nb^{5+} species.[32,35] Continuous cycling and the associated repetitive stress of lithium insertion and deinsertion lead to fatigue of the T-Nb_2O_5 lattice culminating in a collapse of the orthorhombic structure and the formation of an amorphous Nb_2O_5. The resulting inhomogeneity of Nb centers accounts for the increased line width of the Nb 3d peaks after being cycled 10,000 times.

Second, a progressive loss of T-Nb_2O_5 is occurring as a consequence of pitting (Figure 5) and, potentially, dissolution of the film as more soluble Nb^{4+} dissolves into the electrolyte during cycling, leaving behind less-soluble Nb^{5+} of the delithiated oxide. To corroborate this hypothesis, XPS was used to examine the composition of salts recovered by evaporation from the electrolyte used for lithiating/delithiating T-Nb_2O_5 films for 10,000 cycles (Figure 8). There is overlap between the regions where Nb 3d peaks and Cl 2p peaks from the perchlorate salt used as the electrolyte appear; however, the Nb $3d_{5/2}$ peak and the O 1s lattice O^{2-} peak are observed at 206.7 and 533.2 eV, respectively, with the former being characteristic of Nb^{4+} species.[36] This supports the hypothesis that Nb^{4+} is selectively dissolved from the film into the electrolyte.

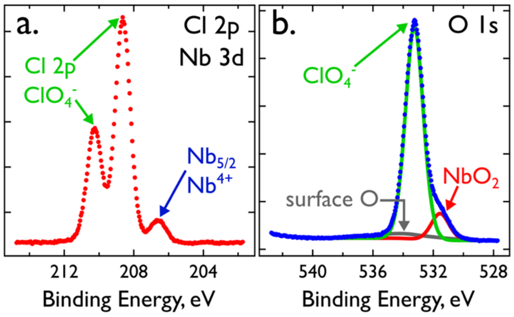

Figure 8. XPS analysis of dissolved salts recovered from the electrolyte after 10,000 cycles. (a). Overlapping Cl 2p and Nb 3d regions showing both Cl 2p peaks consistent with ClO_4^- and Nb^{4+} peaks. (b) O 1s region with deconvolutions illustrating contributions from surface oxygen, ClO_4^-, and NbO_2, as indicated.

Degradation and the Niobium Coordination Sphere: *Ex Situ* Raman Spectroscopy.

There is extensive literature on crystal disorders and phase changes observed in the Raman spectra of niobium oxides.[37−39] Amorphous niobia consists of distorted NbO_6, NbO_7, and NbO_8 polyhedra, characterized by strong and broad stretching modes at or about 650 cm^{-1} in the Raman spectrum.[40] Crystalline niobia are characterized by Nb−O−Nb stretching at 690 cm^{-1}, with sharper transitions than those seen for the amorphous phase, since a majority of the polyhedra are NbO_6 and a minority of polyhedra have distorted coordination. Raman spectral evolution of lithiated and delithiated T-Nb_2O_5 performed by Liu and co-workers[41] showed a weakening of signal intensity between 570 and 770 cm^{-1} upon lithiation. They suggest that this attenuation is due to Li^+ "bridging" Nb−O−Nb oxygens across layers, confirming that Raman bands in the 570−770 cm^{-1} region correspond to Nb−O−Nb stretching.[41]

The influence of the repetitive stress imposed by many lithiation/delithiation cycles on the stretching frequencies of niobia, however, has not been intensively investigated. However, the influence of another mode of damage, mechanical milling, was studied by Senna and co-workers.[42] Starting with pure monoclinic Nb_2O_5, damage by milling induced a softening of the Nb−O−Nb stretch by up to 10 cm^{-1} coupled with an increase in its full width at half maxima (fwhm).[42] Figure 9a shows the progress of niobium pentoxide degradation monitored via Raman spectroscopy, at regular intervals from pristine to 10,000 cycles. The 60 nm T-Nb_2O_5 film was deposited on a 600 nm FTO layer on glass. The glass layer shows a vibration at 560 cm^{-1} (shown in blue), and vibrations of the FTO appear at 600 and 630 cm^{-1} (shown in green) along with a weak vibration near 680 cm^{-1} (shown in

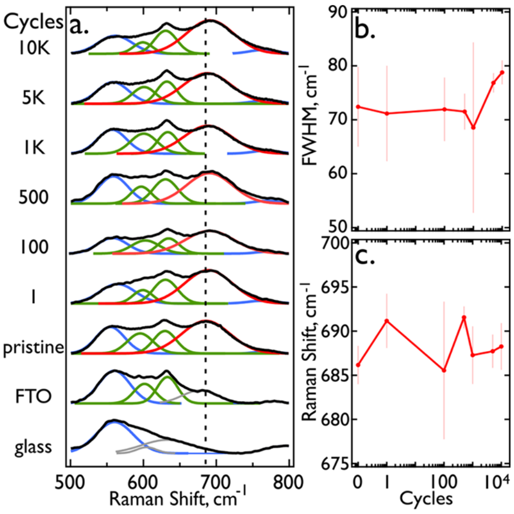

Figure 9. Degradation of the T-Nb_2O_5 coordination sphere upon cycling of a 60 nm T-Nb_2O_5 film deposited on FTO on glass to 10,000 cycles, monitored via *ex situ* Raman spectroscopy. (a) Raman spectra at different intervals of cycling left at a delithiating potential. The blue curve depicts the stretching vibrations for the glass substrate, green for FTO, and red for the Nb−O−Nb stretching vibrations. Gray curves in glass spectra correspond to weak stretching vibrations that are more prominent in the FTO spectra, and the gray curve in the FTO spectra notes a weak stretching vibration in the FTO that is hidden by the Nb−O−Nb stretching vibration. (b,c) Changes in the fwhm and Raman shift of the Nb-O-Nb band, respectively, across 10,000 cycles measured across several regions of the films.

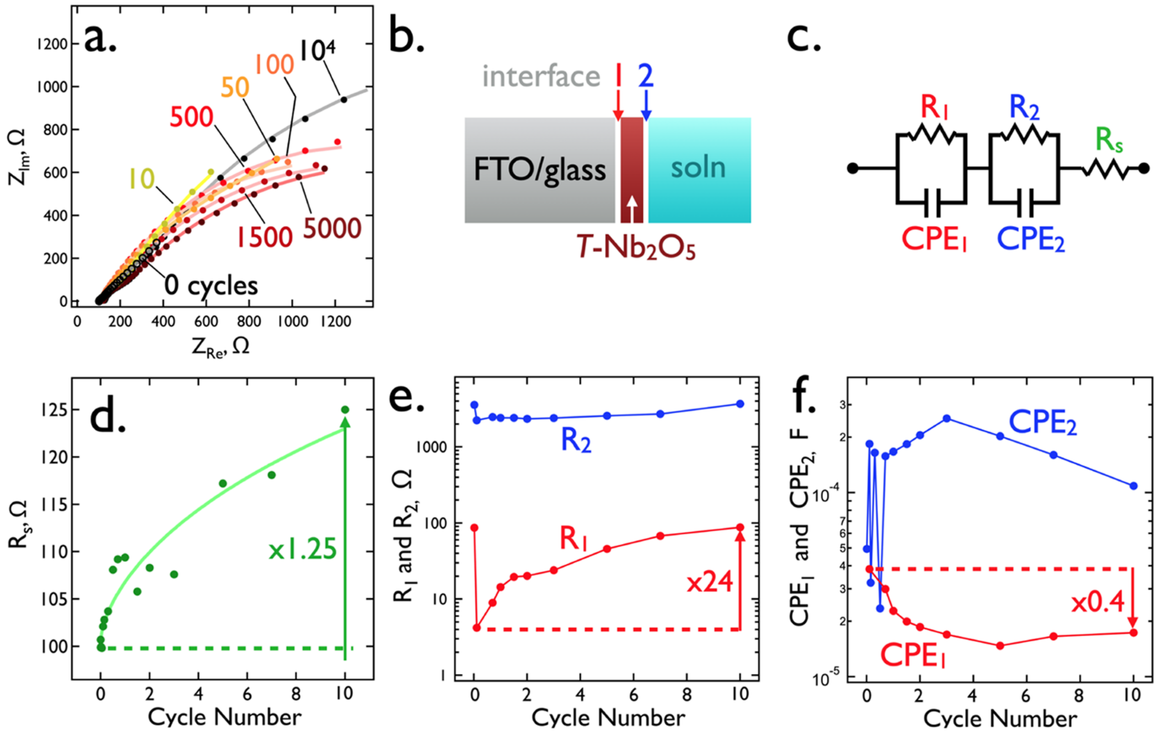

Figure 10. EIS analysis of T-Nb_2O_5 films. (a). Nyquist plots of EIS frequency spectra acquired from 1 Hz to 30 kHz for the delithiated state of T-Nb_2O_5 films in 1.0 M $LiClO_4$, PC. Voltammetric scanning at a rate of 200 mV/s for this film was interrupted at 16 junctures, and EIS spectra were acquired. Data from eight data sets are shown here for clarity. The solid lines are least squares fits to the equivalent circuit model shown in (c). (b) Schematic diagram showing the system under investigation; (c) equivalent circuit used to model the EIS response of a T-Nb_2O_5 film on FTO. (d) R_s *vs* number of cycles. (e). Log-linear plots of the resistances R_1 and R_2. (f). Log-linear plots of the CPEs CPE_1 and CPE_2. Cycle numbers in panels d-f are shown in intervals of 1000 cycles.

gray) that was not seen in the Nb_2O_5 films (Figure 9a). Pristine, uncycled orthorhombic Nb_2O_5 shows an average stretching vibration band at 686 cm^{-1} with an fwhm of 72 cm^{-1}, and changes in these values are tracked across the 10,000 cycles (Figure 9b,c).

The fwhm of the Nb−O−Nb stretching band (Figure 9b) increases significantly (up to 7 cm^{-1}) after 1000−2000 cycles. This is attributed to an increase in the inhomogeneity of the polyhedra in these degraded films. The increase in fwhm coincides with TEM images that show strong distortions of the orthorhombic structure, also at 2000 cycles (Figure 2c). With cycling, the Nb−O−Nb stretching peak shift fluctuates about 5 cm^{-1} (Figure 9c), but it remains in the range from 685 to 692 cm^{-1}, providing no definitive evidence for a change in bond order within the T-Nb_2O_5. Large error bars in both (Figure 9b) and (Figure 9c) indicate inhomogeneity of these quantities across a single sample. This makes the subtle changes in the Raman spectra difficult to precisely track due to interfering spectra of the FTO substrate, especially the small vibration around 680 cm^{-1}, but these data suggest that the coordination sphere of T-Nb_2O_5 becomes more distorted as the film is cycled.

EIS. In contrast to the other techniques employed in this study, EIS was used as an *in situ* rather than an *ex situ* probe of the electronic and electrochemical properties of T-Nb_2O_5 films during cycling.[43] EIS has been used to study Nb_2O_5 battery electrodes[44,45] and supercapacitor[33,46−48] systems, but its application to degradation analysis has not yet been reported to our knowledge. A simple two-interface circuit provides excellent fits to our EIS data across all 10,000 scans (Figure 10a−c). This circuit accounts for the impedance contributions of two interfaces with parallel capacitor−resistor pairs: the FTO/T-Nb_2O_5 interface (interface 1) and the T-Nb_2O_5/solution interface (interface 2). In addition, a solution resistance, R_s, is included in series. Constant phase element (CPE) approximations of a capacitor are used in this analysis.[43]

Nyquist plots acquired at seven frequencies (Figure 10a) consist of two fused semicircles that are well modeled by this equivalent circuit (solid lines, Figure 10a). However, stable values for the circuit elements R_1, CPE_1, R_2, and CPE_2 are not obtained until after ≈100 cycles. The initial impedance response is characterized by highly fluxional values for all four circuit elements, as seen, for example, in the <1000 cycle data of CPE_2 (Figure 10f). This impedance instability is attributed to the mechanical delamination of the T-Nb_2O_5 film from the FTO surface, as documented by the TEM cross sections in Figure 4. As indicated above, we speculate that delamination is the result of the relief of strain between the FTO and T-Nb_2O_5 imposed by lithiation volume expansion of the T-Nb_2O_5. Once delamination has occurred and this strain is relieved, impedance noise disappears and high signal-to-noise impedance data are obtained (Figure 10e,f).

Delamination is expected to increase R_1 as electrical continuity between the FTO and the T-Nb_2O_5 film is lost and to decrease CPE_1 by increasing the effective "capacitor spacing" as the FTO and T-Nb_2O_5 film surfaces are progressively separated from one another. These two changes are observed in the data of Figure 10e,f that document an increase in R_1 by a factor of 24 and a decrease in CPE_1 by 40%.

Changes in R_2 and CPE_2, the culmination of a loss in crystallinity by the T-Nb_2O_5 film, are somewhat more difficult to rationalize. The conversion of a crystalline T-Nb_2O_5 film to an amorphous one should increase R_2, and this is clearly observed: R_2 increases substantially, by 48%, from 2.5 to 3.7 kΩ from 100 to 10,000 cycles (Figure 10e). CPE_2, on the other hand, increases from 1.5×10^{-4} F at 1000 to 2.5×10^{-4} F at 2000 cycles, but with continued cycling, CPE_2 declines to 1.0×10^{-4} F at 10,000 cycles. The source of the noise seen in the CPE_2 data for <1000 cycles is likely caused by the delamination of the film from the FTO.

Finally, the solution resistance, R_s, stays almost constant throughout 10,000 scans, increasing by just 25% (Figure 10d). In view of the magnitude of the changes in the other circuit elements measured here, this change is inconsequential.

How will the observed changes to these five circuit elements influence the performance of T-Nb_2O_5 films? To answer this question, it is important to appreciate that even at the rapid, 200 mV/s scan rate and a 1.8 V voltage window, the effective frequency is just 0.06 Hz—considerably lower than the 1 Hz lowest frequency measured in this study. Therefore, in terms of impacting the energy storage performance of these films, the low frequency impedance provides the most direct measure of impact. The total film impedance, Z_{total} at 1 Hz, encompassing the capacitive (Z_{im}) and the resistive (Z_{re}) impedance components ($Z_{total} = (Z_{im}{}^2 + Z_{re}{}^2)^{1/2}$), increases from 780 Ω at 10 cycles to 1860 Ω at 10,000 cycles (data visible in Figure S2). Therefore, the approximate doubling of the Z_{total} coincides with a reduction in C_{sp} by one-half (from ≈400 to ≈200 C/g, Figure 3b), quantitatively as expected.

CONCLUSIONS

We report the characterization as a function of the number of lithiation/delithiation cycles of ultrathin (60 nm) T-Nb_2O_5 films prepared by EPD. Many (>100) identical films were prepared and characterized using *ex situ* tools including TEM, SEM, EDS, GIXRD, XPS, Raman microprobe spectroscopy, cyclic voltammetry, and (*in situ*) EIS. The main conclusions of this work are the following:

The as-prepared T-Nb_2O_5 films prepared by EPD exhibit high C_{sp} in the 400 F/g range approaching the theoretically expected maximum value of 403 F/g and highly reversible electrical energy storage, retaining significant C_{sp} for up to 10,000 cycles and losing approximately 50% over this number of scans (see data in Figure 2b).

After 1000 lithiation/delithiation cycles, the crystalline, orthorhombic lattice begins to undergo degradation, with numerous lattice distortions visible at 2000 cycles (Figure 2c). This is the interval of scans over which most of the C_{sp} loss occurs. Delamination of the T-Nb_2O_5 film from the FTO current collector producing an appreciable gap is observed (Figure 4). SEM/EDS images of the film surfaces show circular pitting with complete loss of Nb signal within these regions (Figure 5). An inhomogeneity develops in the coordination sphere of oxygens about Nb centers, and NbO_7 and NbO_8 coordinations are observed along with NbO_6 characteristic of T-Nb_2O_5 (Figure 9). This leads to destruction of the low energy barrier pathways for Li^+ intercalation, which comprises the corner-shared NbO_6 octahedra.

In addition to impeding Li^+ diffusion, these chemical changes increase the barrier for electrons to reach the Nb centers, resulting in increased electrical resistance. This increased resistance is directly measured by EIS, which shows significant increases in both R_1 and R_2 (Figure 10) commencing at 1000 cycles.

T-Nb_2O_5 films are largely rendered amorphous at 2000 cycles, and the deleterious changes in film resistance (Figure 10) and chemical state (Figures 7 and 9) continue to be observed. This is direct evidence for the selective leaching of Nb^{4+} from the film (Figure 8). At 10,000 cycles, chemical shifts for Nb 3d and O 1s return to values seen for freshly deposited, amorphous Nb_2O_5 films (i.e., purely Nb^{5+}) prior to annealing. This means that these films are nearly depleted of Nb^{4+}, formed during lithiation.

Remarkably, in spite of the damage documented by these data after 10,000 cycles, the amorphous Nb_2O_5 films retain a $C_{sp} \approx 200$ F/g or 50% of the capacity of freshly annealed and crystalline T-Nb_2O_5 films of $C_{sp} \approx 400$ F/g.

EXPERIMENTAL METHODS

Chemicals and Materials. Niobium pentachloride ($NbCl_5$, 99%), hydrogen peroxide solution (H_2O_2, 30% (w/w) in H_2O), lithium perchlorate ($LiClO_4$, battery grade, dry, 99.99% trace metal basis), propylene carbonate (anhydrous, 99.7%), and FTO-coated glass slides (surface resistivity ≈ 13 Ω/sq) were all used as received from Sigma-Aldrich. FTO was cleaned using a commercial cleaning solution, Hellmanex 3, obtained from Hellma Analytics. The positive photoresist (Shipley S1808) and developer (Shipley MF-319) were purchased from Kayaku Advanced Materials. Acetone and methanol (ACS certified grade) were used as received from Fisher Scientific.

EPD of T-Nb_2O_5. EPD of T-Nb_2O_5 films on FTO was carried out as previously described.[19] Briefly, a modification of the method of Zhitomirsky[49] was used in which a clear, colloidal NbO_x solution was first prepared by rapidly injecting Nb^{5+} in methanol (135 mg of $NbCl_5$ dissolved in 4 mL of methanol) into cold (≈2 °C) hydrogen peroxide. After aging at room temperature for 3 h, EPD was carried out potentiostatically on a 6 × 6 mm FTO electrode with an area of 0.36 cm^2 in the two-electrode mode at −2.0 V. Under these conditions, a quasi-constant deposition current was measured and EPD was continued until a total Coulombic loading of 1.4 C/cm^2 was obtained—approximately 190 s. T-Nb_2O_5 films of 60 nm in thickness were then obtained by calcination at 600 °C for 8 h.

Electrochemical Characterization. All electrochemical measurements were performed by a one-compartment three-electrode cell using a Gamry Series G 300 potentiostat. Cyclic voltammetry was conducted in 1.0 M $LiClO_4$ (battery grade, dry, 99.99%) in dry propylene carbonate inside a N_2 glovebox. A glassy carbon rod (2 mm diameter) was used as the counter electrode with a platinum wire pseudoreference electrode for the electrochemical measurements. EIS measurements were conducted from 1 Hz to 30 kHz using an amplitude of 10 mV. All potentials are referenced to the Li/Li^+ couple, $E_{Li/Li^+} = -3.045$ V *versus* normal hydrogen electrode,[50] by calibrating the Pt pseudoreference electrode against Li/Li^+ using ferrocene/ferrocenium ($Fc/Fc^{+\cdot}$) in 1.0 M $LiClO_4$, PC.[51]

Structural Characterization. SEMs and EDS were acquired using an FEI Magellan 400 XHR system equipped with an Oxford Instruments EDS detector (80 mm^2, AZtec software). Before imaging, samples were sputter-coated with ≈5 nm of iridium. Accelerating voltages of incident electron beams ranged from 10 to 30 kV, and probe currents ranged from 25 pA to 0.4 nA. All SEM specimens were mounted on stainless steel stubs and held by carbon tape. XPS was measured using the AXIS Supra by Kratos Analytical Inc. equipped with a monochromatic Al/Ag X-ray source. Raman spectra were obtained using a customized Renishaw InVia Raman microscope with a 532 nm excitation laser with a 2 μm spot size. Raman transitions were fit to Gaussians to extract peak positions and the fwhm. GIXRD patterns were collected using a Rigaku SmartLab X-ray diffractometer in parallel beam geometry with a fixed incident angle of 0.3°. The Cu K_α X-ray generator was operated at 40 kV and 44 mA.

TEM. TEM was performed on a JEOL JEM 2800 transmission electron microscope equipped with a 200 kV Schottky field-emission electron gun. High-resolution TEM images were recorded at a resolution of 0.2 nm. FFTs were taken from selected areas in the high-resolution TEM images.

■ ASSOCIATED CONTENT

Supporting Information

The Supporting Information is available free of charge at https://pubs.acs.org/doi/10.1021/acsaem.1c00580.

SEM and EDS images of Nb and O in the 1000 cycle film and an extended Nyquist plot of the data shown in Figure 9a to show the total film impedance at 1 Hz for 10,000 cycles (PDF)

■ AUTHOR INFORMATION

Corresponding Authors

Xiaoqing Pan − *Department of Materials Science and Engineering, University of California, Irvine, California 92697, United States;* orcid.org/0000-0002-0965-8568; Email: xpan@uci.edu

Reginald M. Penner − *Department of Chemistry, University of California, Irvine, California 92697, United States;* orcid.org/0000-0003-2831-3028; Email: rmpenner@uci.edu

Authors

Ilektra Andoni − *Department of Chemistry, University of California, Irvine, California 92697, United States*

Joshua M. Ziegler − *Department of Chemistry, University of California, Irvine, California 92697, United States*

Gaurav Jha − *Department of Chemistry, University of California, Irvine, California 92697, United States;* orcid.org/0000-0003-4590-2473

Chaitanya Avinash Gadre − *Department of Materials Science and Engineering, University of California, Irvine, California 92697, United States*

Heriberto Flores-Zuleta − *Department of Chemistry, University of California, Irvine, California 92697, United States*

Sheng Dai − *Department of Materials Science and Engineering, University of California, Irvine, California 92697, United States;* orcid.org/0000-0001-5787-0179

Shaopeng Qiao − *Department of Chemistry, University of California, Irvine, California 92697, United States*

Mingjie Xu − *Department of Materials Science and Engineering, University of California, Irvine, California 92697, United States*

Vivian T. Chen − *Department of Chemistry, University of California, Irvine, California 92697, United States*

Complete contact information is available at: https://pubs.acs.org/10.1021/acsaem.1c00580

Author Contributions

[§]I.A. and J.M.Z. contributed equally to this work.

Notes

The authors declare no competing financial interest.

■ ACKNOWLEDGMENTS

This work was supported by the National Science Foundation though proposal CBET 1803314 (R.M.P.) and 2031494 (X.P.) and partially supported through the UCI MRSEC DMR-2011967. Valuable discussions with Professors Phil Collins (UCI), Zuzanna Siwy (UCI), Bruce Dunn (UCLA), and their students are gratefully acknowledged. SEM, TEM, XRD, and XPS data were acquired at the Irvine Materials Research Institute (IMRI, imri.uci.edu) at UCI. Raman data were acquired at the Laser Spectroscopy Labs at UCI (https://www.chem.uci.edu/~dmitryf/index.html).

■ REFERENCES

(1) Birkl, C. R.; Roberts, M. R.; McTurk, E.; Bruce, P. G.; Howey, D. A. Degradation Diagnostics for Lithium Ion Cells. *J. Power Sources* **2017**, *341*, 373−386.

(2) Dixit, M.; Markovsky, B.; Schipper, F.; Aurbach, D.; Major, D. T. Origin of Structural Degradation during Cycling and Low Thermal Stability of Ni-Rich Layered Transition Metal-Based Electrode Materials. *J. Phys. Chem. C* **2017**, *121*, 22628−22636.

(3) Han, X.; Lu, L.; Zheng, Y.; Feng, X.; Li, Z.; Li, J.; Ouyang, M. A Review on the Key Issues of the Lithium Ion Battery Degradation among the Whole Life Cycle. *eTransportation* **2019**, *1*, 100005.

(4) Pender, J. P.; Jha, G.; Youn, D. H.; Ziegler, J. M.; Andoni, I.; Choi, E. J.; Heller, A.; Dunn, B. S.; Weiss, P. S.; Penner, R. M.; Mullins, C. B. Electrode Degradation in Lithium-Ion Batteries. *ACS Nano* **2020**, *14*, 1243−1295.

(5) Zhang, S.; Zhao, K.; Zhu, T.; Li, J. Electrochemomechanical Degradation of High-Capacity Battery Electrode Materials. *Prog. Mater. Sci.* **2017**, *89*, 479−521.

(6) Kong, L.; Zhang, C.; Wang, J.; Qiao, W.; Ling, L.; Long, D. Free-Standing T-Nb_2O_5/Graphene Composite Papers with Ultrahigh Gravimetric/Volumetric Capacitance for Li-ion Intercalation Pseudocapacitor. *ACS Nano* **2015**, *9*, 11200−11208.

(7) Kong, L.; Zhang, C.; Wang, J.; Qiao, W.; Ling, L.; Long, D. Nanoarchitectured Nb_2O_5 Hollow, Nb_2O_5@Carbon and NbO_2@Carbon Core-Shell Microspheres for Ultrahigh-Rate Intercalation Pseudocapacitors. *Sci. Rep.* **2016**, *6*, 21177.

(8) Lim, E.; Jo, C.; Kim, H.; Kim, M.-H.; Mun, Y.; Chun, J.; Ye, Y.; Hwang, J.; Ha, K.-S.; Roh, K. C.; Kang, K.; Yoon, S.; Lee, J. Facile Synthesis of Nb_2O_5@Carbon Core-Shell Nanocrystals with Controlled Crystalline Structure for High-Power Anodes in Hybrid Supercapacitors. *ACS Nano* **2015**, *9*, 7497−7505.

(9) Wang, X.; Li, G.; Chen, Z.; Augustyn, V.; Ma, X.; Wang, G.; Dunn, B.; Lu, Y. High-Performance Supercapacitors Based on Nanocomposites of Nb_2O_5 Nanocrystals and Carbon Nanotubes. *Adv. Energy Mater.* **2011**, *1*, 1089−1093.

(10) Wang, J.; Li, H.; Shen, L.; Dong, S.; Zhang, X. Nb_2O_5 nanoparticles encapsulated in ordered mesoporous carbon matrix as advanced anode materials for Li ion capacitors. *RSC Adv.* **2016**, *6*, 71338−71344.

(11) Luo, G.; Li, H.; Zhang, D.; Gao, L.; Lin, T. A Template-Free Synthesis via Alkaline Route for Nb_2O_5/Carbon Nanotubes Composite as Pseudo-Capacitor Material with High-Rate Performance. *Electrochim. Acta* **2017**, *235*, 175−181.

(12) Wang, L. P.; Yu, L.; Satish, R.; Zhu, J.; Yan, Q.; Srinivasan, M.; Xu, Z. High-Performance Hybrid Electrochemical Capacitor with Binder-Free $Nb_2O_5$5@Graphene. *RSC Adv.* **2014**, *4*, 37389−37394.

(13) Li, H.; Zhu, Y.; Dong, S.; Shen, L.; Chen, Z.; Zhang, X.; Yu, G. Self-Assembled Nb_2O_5 Nanosheets for High Energy−High Power Sodium Ion Capacitors. *Chem. Mater.* **2016**, *28*, 5753−5760.

(14) Lai, C.-H.; Ashby, D.; Moz, M.; Gogotsi, Y.; Pilon, L.; Dunn, B. Designing Pseudocapacitance for Nb_2O_5/Carbide-Derived Carbon Electrodes and Hybrid Devices. *Langmuir* **2017**, *33*, 9407−9415.

(15) Kim, J. W.; Augustyn, V.; Dunn, B. The Effect of Crystallinity on the Rapid Pseudocapacitive Response of Nb_2O_5. *Adv. Energy Mater.* **2012**, *2*, 141−148.

(16) Viet, A. L.; Reddy, M. V.; Jose, R.; Chowdari, B. V. R.; Ramakrishna, S. Nanostructured Nb_2O_5 Polymorphs by Electrospinning for Rechargeable Lithium Batteries. *J. Phys. Chem. C* **2009**, *114*, 664−671.

(17) Muruganantham, R.; Sivakumar, M.; Subadevi, R. Polyol Technique Synthesis of Nb_2O_5 Coated on $LiFePO_4$ Cathode Materials for Li-ion Storage. *Ionics* **2017**, *24*, 989. DOI: 10.1007/s11581-017-2264-x

(18) Griffith, K. J.; Forse, A. C.; Griffin, J. M.; Grey, C. P. High-rate Intercalation without Nanostructuring in Metastable Nb_2O_5 Bronze phases. *J. Am. Chem. Soc.* **2016**, *138*, 8888−8899.

(19) Jha, G.; Tran, T.; Qiao, S.; Ziegler, J. M.; Ogata, A. F.; Dai, S.; Xu, M.; Le Thai, M.; Chandran, G. T.; Pan, X.; Penner, R. M. Electrophoretic Deposition of Mesoporous Niobium(V)Oxide Nanoscopic Films. *Chem. Mater.* **2018**, *30*, 6549−6558.

(20) Augustyn, V.; Come, J.; Lowe, M. A.; Kim, J. W.; Taberna, P.-L.; Tolbert, S. H.; Abruña, H. D.; Simon, P.; Dunn, B. High-rate electrochemical energy storage through Li^+ intercalation pseudocapacitance. *Nat. Mater.* **2013**, *12*, 518−522.

(21) Zhang, C.; Maloney, R.; Lukatskaya, M. R.; Beidaghi, M.; Dyatkin, B.; Perre, E.; Long, D.; Qiao, W.; Dunn, B.; Gogotsi, Y. Synthesis and Electrochemical Properties of Niobium Pentoxide Deposited on Layered Carbide-Derived Carbon. *J. Power Sources* **2015**, *274*, 121−129.

(22) Beidaghi, M.; Zhang, C.; Lukatskaya, M.; Maloney, R.; Dunn, B.; Gogotsi, Y. One-Step Synthesis of Carbon Supported Nb_2O_5 Particles for Electrochemical Capacitor Applications by Oxidation of Layered Nb_2C. *ECS Meet. Abstr.* **2014**, MA2014-02,185.

(23) Come, J.; Augustyn, V.; Kim, J. W.; Rozier, P.; Taberna, P.-L.; Gogotsi, P.; Long, J. W.; Dunn, B.; Simon, P. Electrochemical Kinetics of Nanostructured Nb_2O_5 Electrodes. *J. Electrochem. Soc.* **2014**, *161*, A718−A725.

(24) Yan, Y.; Lai, C.-H.; Robbennolt, S.; Dunn, B.; Tolbert, S. *Nb_4N_5/Nb_2O_5-rGO Composites as Pseudocapacitive Anode Materials for High Power Lithium Ion Batteries*; Abstracts of Papers of the American Chemical Society, 2017.

(25) Ohzuku, T.; Sawai, K.; Hirai, T. Electrochemistry of L-Niobium Pentoxide A Lithium/Non-Aqueous Cell. *J. Power Sources* **1987**, *19*, 287−299.

(26) Lou, S.; Cheng, X.; Wang, L.; Gao, J.; Li, Q.; Ma, Y.; Gao, Y.; Zuo, P.; Du, C.; Yin, G. High-Rate Capability of Three-Dimensionally Ordered Macroporous T-Nb_2O_5 through Li^+ Intercalation Pseudocapacitance. *J. Power Sources* **2017**, *361*, 80−86.

(27) Elangovan, E.; Ramamurthi, K. Studies on micro-structural and electrical properties of spray-deposited fluorine-doped tin oxide thin films from low-cost precursor. *Thin Solid Films* **2005**, *476*, 231−236.

(28) Kumagai, N.; Koishikawa, Y.; Komaba, S.; Koshiba, N. Thermodynamics and Kinetics of Lithium Intercalation into Nb_2O_5 Electrodes for a 2 V Rechargeable Lithium Battery. *J. Electrochem. Soc.* **1999**, *146*, 3203−3210.

(29) Yan, L.; Chen, G.; Sarker, S.; Richins, S.; Wang, H.; Xu, W.; Rui, X.; Luo, H. Ultrafine Nb_2O_5 Nanocrystal Coating on Reduced Graphene Oxide as Anode Material for High Performance Sodium Ion Battery. *ACS Appl. Mater. Interfaces* **2016**, *8*, 22213−22219.

(30) Kumagai, N.; Tanno, K.; Nakajima, T.; Watanabe, N. Structural Changes of Nb_2O_5 and V_2O_5 as Rechargeable Cathodes for Lithium Battery. *Electrochim. Acta* **1983**, *28*, 17−22.

(31) Öezer, N.; Barreto, T.; Bueyueklimanli, T.; Lampert, C. M. Characterization of Sol-Gel Deposited Niobium Pentoxide Films for Electrochromic Devices. *Sol. Energy Mater. Sol. Cells* **1995**, *36*, 433−443.

(32) Coşkun, Ö.; Demirel, S.; Atak, G. The Effects of Heat Treatment on Optical, Structural, Electrochromic and Bonding Properties of Nb_2O_5 Thin Films. *J. Alloys Compd.* **2015**, *648*, 994−1004.

(33) Zhang, S.; Liu, G.; Qiao, W.; Wang, J.; Ling, L. Oxygen Vacancies Enhance the Lithium Ion Intercalation Pseudocapacitive Properties of Orthorhombic Niobium Pentoxide. *J. Colloid Interface Sci.* **2020**, *562*, 193−203.

(34) Lee, K.; Kim, J.; Mok, I.-S.; Na, H.; Ko, D.-H.; Sohn, H.; Lee, S.; Sinclair, R. RESET-First Unipolar Resistance Switching Behavior in Annealed Nb_2O_5 Films. *Thin Solid Films* **2014**, *558*, 423−429.

(35) Cava, R. J.; Batlogg, B.; Krajewski, J. J.; Poulsen, H. F.; Gammel, P.; Peck, W. F., Jr; Rupp, L. W., Jr Electrical and Magnetic Properties of $Nb_2O_{5-\delta}$ Crystallographic Shear Structures. *Phys. Rev. B: Condens. Matter Mater. Phys.* **1991**, *44*, 6973.

(36) Aufray, M.; Menuel, S.; Fort, Y.; Eschbach, J.; Rouxel, D.; Vincent, B. New Synthesis of Nanosized Niobium Oxides and Lithium Niobate Particles and Their Characterization by XPS Analysis. *J. Nanosci. Nanotechnol.* **2009**, *9*, 4780−4785.

(37) Pittman, R. M.; Bell, A. T. Raman Studies of the Structure of Niobium Oxide/Titanium Oxide (Nb_2O_5/TiO_2). *J. Phys. Chem.* **1993**, *97*, 12178−12185.

(38) McConnell, A. A.; Aderson, J. S.; Rao, C. N. R. Raman Spectra of Niobium Oxides. *Spectrochim. Acta, Part A* **1976**, *32*, 1067−1076.

(39) Hardcastle, F.; Wachs, I. Determination of Niobium-Oxygen Bond Distances and Bond Orders by Raman Spectroscopy. *Solid State Ionics* **1991**, *45*, 201−213.

(40) Jehng, J. M.; Wachs, I. E. Structural Chemistry and Raman Spectra of Niobium Oxides. *Chem. Mater.* **1991**, *3*, 100−107.

(41) Chen, D.; Wang, J.-H.; Chou, T.-F.; Zhao, B.; El-Sayed, M. A.; Liu, M. Unraveling the Nature of Anomalously Fast Energy Storage in T-Nb2O5. *J. Am. Chem. Soc.* **2017**, *139*, 7071−7081.

(42) Ikeya, T.; Senna, M. Change in the Structure of Niobium Pentoxide due to Mechanical and Thermal Treatments. *J. Non-Cryst. Solids* **1988**, *105*, 243−250.

(43) Bredar, A. R. C.; Chown, A. L.; Burton, A. R.; Farnum, B. H. Electrochemical Impedance Spectroscopy of Metal Oxide Electrodes for Energy Applications. *ACS Appl. Energy Mater.* **2020**, *3*, 66−98.

(44) Aricò, A. S.; Bruce, P.; Scrosati, B.; Tarascon, J.-M.; Van Schalkwijk, W. Nanostructured Materials for Advanced Energy Conversion and Storage Devices. *Nat. Mater.* **2005**, *4*, 366−377.

(45) Qian, S.; Yu, H.; Yan, L.; Zhu, H.; Cheng, X.; Xie, Y.; Long, N.; Shui, M.; Shu, J. High-Rate Long-Life Pored Nanoribbon VNb_9O_{25} Built by Interconnected Ultrafine Nanoparticles as Anode for Lithium-Ion Batteries. *ACS Appl. Mater. Interfaces* **2017**, *9*, 30608−30616.

(46) Zhang, J.; Chen, H.; Sun, X.; Kang, X.; Zhang, Y.; Xu, C.; Zhang, Y. High Intercalation Pseudocapacitance of Free-Standing T-Nb_2O_5 Nanowires@Carbon Cloth Hybrid Supercapacitor Electrodes. *J. Electrochem. Soc.* **2017**, *164*, A820.

(47) Wang, X.; Li, G.; Tjandra, R.; Fan, X.; Xiao, X.; Yu, A. Fast Lithium-Ion Storage of Nb_2O_5 Nanocrystals *In Situ* Grown on Carbon Nanotubes for High-Performance Asymmetric Supercapacitors. *RSC Adv.* **2015**, *5*, 41179−41185.

(48) Wang, L.; Bi, X.; Yang, S. Partially Single-Crystalline Mesoporous Nb_2O_5 Nanosheets in between Graphene for Ultrafast Sodium Storage. *Adv. Mater.* **2016**, *28*, 7672−7679.

(49) Zhitomirsky, I. Electrolytic Deposition of Niobium Oxide Films. *Mater. Lett.* **1998**, *35*, 188−193.

(50) Bard, A. J.; Faulkner, L. R. *Electrochemical Methods: Fundamentals and Applications*, 2nd ed.; Wiley: New York, 2001.

(51) Laoire, C. O.; Plichta, E.; Hendrickson, M.; Mukerjee, S.; Abraham, K. M. Electrochemical Studies of Ferrocene in a Lithium Ion Conducting Organic Carbonate Electrolyte. *Electrochim. Acta* **2009**, *54*, 6560−6564.

https://doi.org/10.1021/acsaem.1c00580
ACS Appl. Energy Mater. 2021, 4, 6542−6552